npj | computational materials

Article

Published in partnership with the Shanghai Institute of Ceramics of the Chinese Academy of Sciences

https://doi.org/10.1038/s41524-025-01716-0

Two-dimensional Weyl and type-III Dirac semimetals in BaCu monolayer and twisted α/β-BaCu/BN systems

Yiwei Liang[1], Xinyan Lin[2], Biao Wan[3] ✉, Yujin Jia[4], Yuting Qian[5,6,7], Dexi Shao[2] ✉ & Huiyang Gou[1] ✉

Two-dimensional (2D) topological insulators with symmetry-protected helical edge states have drawn significant interest. The recently synthesized layered 2D electride BaCu features a monolayer structure with intriguing band crossings near Fermi level and a low exfoliation energy. In this study, first-principles calculations combined with symmetry analysis reveal that the BaCu monolayer behaves as a 2D topological insulator (TI) nature. When integrated with a 30° twisted $\sqrt{3} \times \sqrt{3}$ hexagonal boron nitride (h-BN) supercell, the resulting twisted α/β-BaCu/BN heterobilayers exhibit 2D Weyl points and type-III Dirac points, respectively, demonstrating that twist angle can effectively modulate topological properties. Interestingly, ab initio molecular dynamics (AIMD) simulations reveal a spontaneous transition from the metastable β-BaCu/BN to α-BaCu/BN configuration, indicating a low energy barrier and highlighting the potential for property modulation, emphasizing the versatility of twisted structures for tuning topological states. This work establishes a robust platform for exploring twist-angle-induced topological electride states, broadening the scope for future investigations.

Two-dimensional (2D) materials, consisting of atomically thin sheets, have garnered significant attention since the discovery of graphene[1,2], largely due to their remarkable properties. Notable examples include the Dirac cone in graphene, valley-selective light absorption in 2D transition metal dichalcogenides (TMDs), and the exceptional insulation offered by hexagonal boron nitride (h-BN) nanolayers[3–5]. The weak van der Waals (vdW) interactions between adjacent layers allow for tunable properties through techniques such as vertical stacking and horizontal twisting of multiple layers[6]. Since the pioneering proposal of magic-angle graphene in refs. 7,8, the deliberate rotation between adjacent layers has become a key strategy to manipulate moiré periodic potentials and interlayer electronic coupling[7–10]. This method not only modifies the intrinsic properties of the constituent layers, but also gives rise to a series of novel interface effect, such as unconventional superconductivity[7,11,12], topological conducting channels[13–16], and other correlated electronic phases. Its application has rapidly gained prominence in the study of 2D materials. As a result, twist-angle control has rapidly established itself as a transformative tool in the exploration of 2D materials and their emergent quantum properties.

Within this category, 2D topological materials—comprising insulators and semimetals—have emerged as a focal point due to their intriguing physics and experimental potential[17–21]. Notably, 2D topological insulators (TIs) exhibit a bulk energy gap and helical edge states, enabling dissipationless transport channels and the quantum spin Hall (QSH) effect[22–25], provided time-reversal symmetry (TRS) remains intact. In particular, the superconductivity and magnetism can be induced through proximity effect, combined with the structural flexibility enabled by vdW interactions, which makes stacked 2D heterostructures a versatile platform for exploring topological phenomena[26–29]. Such as in the heterojunction consists of a graphene single layer sandwiched between two Bi_2Se_3 slabs, the 2D TI character of graphene and the strong SOC effect in Bi_2Se_3 layers lead to a strong band inversion with a large intrinsic bulk band gap[30]. Similarly, 1D topological superconductivity has been demonstrated in the proximity-induced MoS_2 layer by NbS_2[31,32]. These examples highlight how the construction of tailored heterostructures offers an effective strategy for designing and realizing topological quantum materials.

Recently, a layered BaCu electride was synthesized[33], exhibiting a monolayer structure with half-metal conductivity and distinctive band characteristics. Notably, its lower exfoliation energy (~0.84 J/m²) compared to the first 2D electride Ca_2N[34] (~1.11 J/m², obtained via liquid exfoliation[35]) suggests the feasibility of isolating monolayers from the bulk material. As a

[1]Center for High Pressure Science &Technology Advanced Research, Beijing, China. [2]Department of Physics, Hangzhou Normal University, Hangzhou, China. [3]Key Laboratory of Materials Physics of Ministry of Education, School of Physics and Laboratory of Zhongyuan Light, Zhengzhou University, Zhengzhou, China. [4]Beijing National Laboratory for Condensed Matter Physics and Institute of Physics, Chinese Academy of Sciences, Beijing, China. [5]Department of Physics and Astronomy, Seoul National University, Seoul, Korea. [6]Center for Theoretical Physics (CTP), Seoul National University, Seoul, Korea. [7]Institute of Applied Physics, Seoul National University, Seoul, Korea. ✉e-mail: biaowan@zzu.edu.cn; sdx@hznu.edu.cn; huiyang.gou@hpstar.ac.cn

novel layered electride, its monolayer structure exhibits multiple intriguing band crossings near Fermi level (E_F)[33], which may lead to 2D TI behavior while retaining its characteristic electride properties. In this study, we identify the BaCu monolayer as a nodal-line semimetal without SOC, with a nodal ring encircling the K and K′ points, as shown in Fig. 2b. When SOC is introduced, the nodal line is gapped, transforming the BaCu monolayer into a topological metal with 2D TI characteristic. Inspired by recent advancements in twisted bilayer physics[7,8], we also investigate twisted heterostructures combining a BaCu monolayer and a hexagonal boron-nitride (h-BN) monolayer. Our findings reveal that the global minimum α-BaCu/BN configuration hosts six Weyl points, indicative of tunable topological properties. Additionally, the low energy barrier between α-BaCu/BN and local minimum β-BaCu/BN configuration suggests the potential for structural modulation. The β-BaCu/BN system, with Ba and Cu atoms aligned to the honeycomb voids of h-BN, is identified as a Dirac semimetal featuring a nearly flat band crossing the Γ−K line at the E_F. Due to the lack of inversion symmetry, SOC-induced band splitting results in two Weyl points with opposite chirality. The small magnitude of this SOC splitting (~3.9 meV) underscores the robustness of Dirac fermions in the twisted system, highlighting their potential for further exploration in 2D topological materials.

Results and discussions

BaCu monolayer

Figure 1a, b illustrates the crystal structure of the single-layer BaCu in side and top views. The monolayer has a lattice constant of a = b ≈ 4.33 Å and belongs to the *P6/mmm* space group (SG.191), corresponding to the *p6/mmm* layer group (LG.80). The BaCu monolayer consists of a Ba-Cu-Ba triple-layer configuration, with Cu atoms arranged in a hexagonal honeycomb pattern at 2 d Wyckoff positions (0.667, 0.333, 0.5). Ba atoms are located above and below the Cu-honeycomb layer at 2e Wyckoff positions (0, 0, 0.576). Detailed structural parameters, provided in Supplementary Information Table SI, confirm the optimized geometry. The phonon spectrum, free of imaginary frequencies (Fig. S1a), indicates the dynamical stability of the BaCu monolayer. Furthermore, the evolution of total potential energy and the preservation of ground-state geometry during ab initio molecular dynamics (AIMD) simulations over 6 ps at 0 GPa and both 300 K and 700 K (Fig. S1b, c) confirm its thermal stability at ambient and higher temperature conditions.

To elucidate the electronic properties of the BaCu monolayer, the deformation charge density difference (DCDD) and electron localization function (ELF) were analyzed. As shown in Fig. 1c, Ba atoms act as electron donors, while the regions surrounding Cu atoms and their corresponding surface positions serve as electron acceptors. The ELF further corroborates this, revealing an attractor near the (0.333,0.667,0.36) position with a charge density of above 0.4 (Fig. 1d). These attractors are indicative of interstitial anionic electrons (IAEs), suggesting the electride nature. A transverse section plane (S_1) through the IAEs reveals a weak honeycomb-like electronic network (Fig. 1e), which closely resembles the electron distribution observed in the Cu transverse section plane (S_2) (Fig. 1f). This similarity underscores the presence of metallic bonding characteristics. This electronic configuration likely contributes to the low work function (WF) of the BaCu monolayer (calculated value of 2.659 eV), which is lower than the WF of monolayered Ca_2N (3.51 eV) and comparable to Ca_2C (2.45 eV)[36]. Projected density of states (PDOS) analysis in Fig. 2a further confirms the metallic nature of the BaCu monolayer and highlights the strong hybridization between Ba and Cu atoms. Further analysis reveals the Ba-$d_{xy(x^2-y^2)}$ orbital contributes most among *d*-orbitals and shows stronger hybridization with Cu-$d_{xy(x^2-y^2)}$ and Cu-$d_{xz(yz)}$ orbitals. Moreover, the Cu-d_{z^2} orbital shows a relatively localized peak near −0.18 eV in the PDOS, which indicates the Cu-d_{z^2} orbital hosts a visible contribution to the band crossing along K-Γ.

The band structure without SOC, presented in Fig. 2a, reveals a band inversion between Ba-*s* and Cu-*d* orbitals near the K point, resulting in band crossings near the E_F along K-M and K-Γ, respectively. The irreducible representations of the high-symmetry *k*-points, calculated and labeled in Fig. 2a, indicate that these band crossings are protected by M_z symmetry. Given that (k_x, k_y) in the 2D Brillouin zone (BZ) remain invariant under M_z, the M_z-protected band crossings (i.e., the two bands host different mirror eigenvalues $g_z = +1$ and -1) correspond to a one-dimensional nodal line[37], as determined through codimension analysis. The condition for such a nodal line can be described by the equation:

$$E_+\left(\vec{k}\right) = E_-\left(\vec{k}\right) \tag{1}$$

where $\vec{k}$ has two independent components, $E_+\left(\vec{k}\right)$ and $E_-\left(\vec{k}\right)$ denote eigenvalues of the crossing bands with $g_z = +1$ and -1, respectively. This

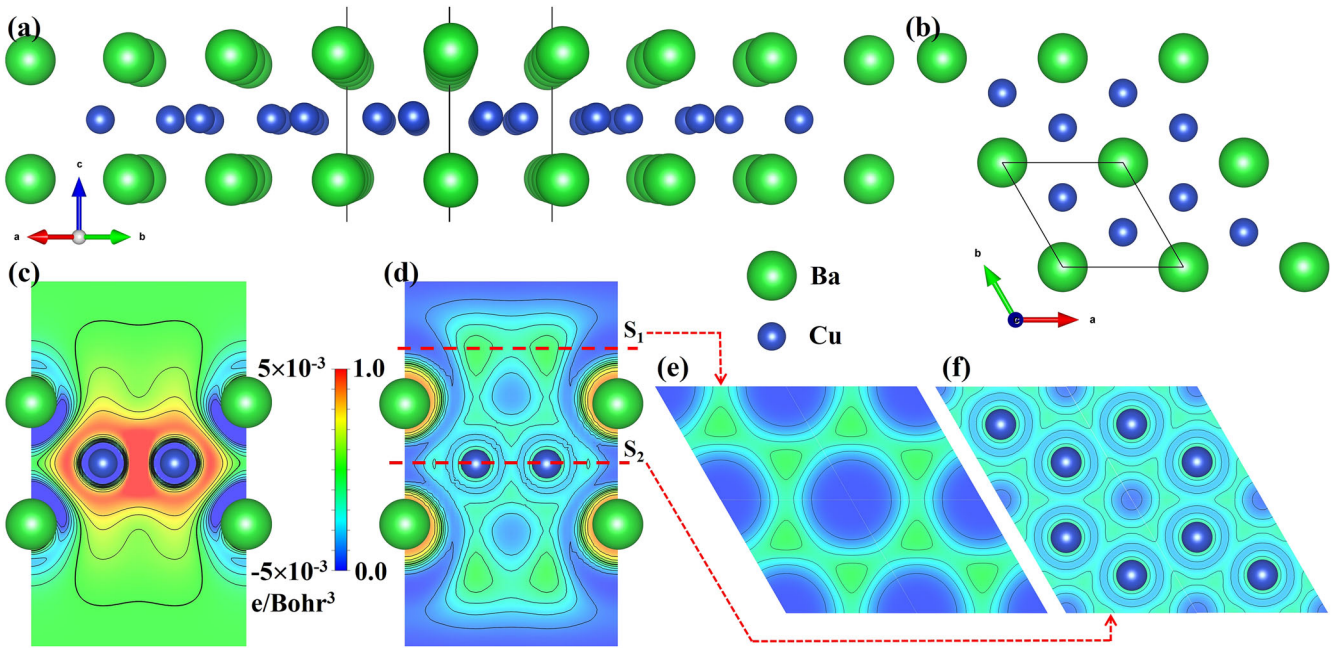

Fig. 1 | Crystal structure and charge distribution analysis of BaCu monolayer. Single layer structure of BaCu with **a** side and **b** top view. **c** DCDD of BaCu monolayer in (110) plane. The ELF contours of BaCu monolayer on the **d** (110), **e** S_1 and **f** S_2 planes with the 0.1 linear divide.

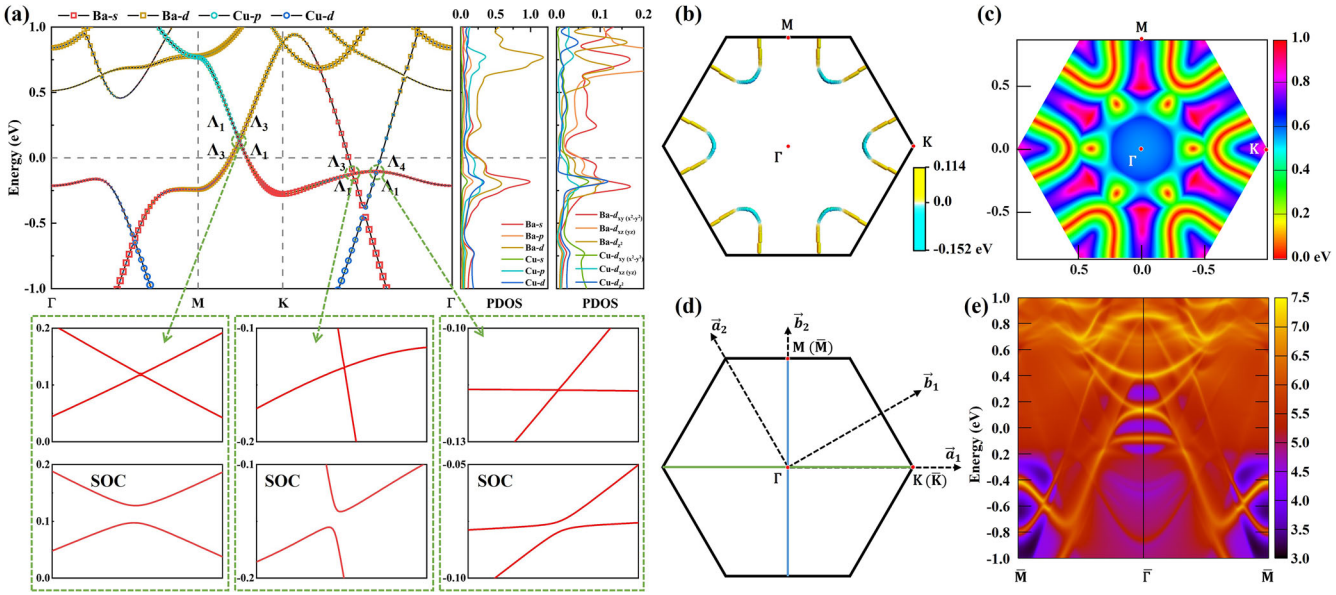

Fig. 2 | Topological band structure and 2D scanning of BaCu monolayer. a The orbital-projected band structure and PDOS (states/eV/f.u.) of BaCu monolayer with the calculated local area band structures without/with SOC. 2D scanning of the **b** nodal line in the BZ and **c** the gap between CBM and VBM for k points. **d** The BZ of BaCu monolayer and α/β-BaCu/BN systems, with the high-symmetry *k*-points indicated. The blue and green lines represent the projection of BZ along [100] and [120] miller index directions, respectively. **e** Edge states of BaCu monolayer in the (010) surface, which exhibits a 2D Dirac cone.

implies that the solution space to the equation is generically one-dimensional, forming a nodal line. To validate this theoretical prediction, a two-dimensional band scan was performed with a 101 × 101 *k* -mesh over 1/6 BZ. The resulting 2D density plots, shown in Fig. 2b, c, clearly exhibit nodal rings encircling both K and K′, confirming the presence of these one-dimensional nodal lines.

SOC is critical for engineering topological states, as demonstrated in phenomena like the QSH effect in graphene[17,22] and $Ta_2M_3Te_5$ (M=Pd, Ni) compounds[38,39] and large-SOC-gap three dimensional topological insulators such as Bi_2Se_3 and NaCaBi families[40,41]. In the BaCu monolayer system, the refined projected band shows a gap opening after considering SOC (Fig. 2a). The inclusion of SOC ensures that P∗T-related degenerate states share the same M_z eigenvalue[42], leading to the gapping of both nodal rings. This SOC-induced band gap around the K-point, as shown in Fig. 2c, is a clear manifestation of this effect. Symmetry eigenvalues, or irreducible representations (irreps), are essential for identifying TIs and topological crystalline insulators (TCIs) in solid systems[43–45]. Since SOC induces a direct band gap at each ***k*** point, the wavefunctions of the N lowest bands (where N corresponds to the number of valence electrons) can be defined throughout the entire 2D BZ, even though the system has a negative indirect band gap. Thus, using the method by Fu and Kane[46], the Z_2 index is calculated by multiplying all the parities for the occupied bands at all time-reversal-invariant momenta (TRIMs). The resultant parity of Γ and M is calculated to be "+" and "−", respectively. Therefore, the calculated topological invariant $Z_2 = 1$, which indicates that the BaCu monolayer exhibits the characteristics of a 2D TI. In the other hand, since the existence of the negative indirect band gap, i.e., there are electron and hole pockets crossing the E_F, the monolayer is a metal. Thus, the BaCu monolayer is a topological metal with $Z_2 = 1$ for the N lowest bands. To identify the nontrivial topological metal phase, we perform the edge state calculations based on a tight-binding model constructed using maximally localized Wannier functions, combined with surface Green's function methods[47,48]. As shown in the projected Brillouin zone (BZ) in Fig. 2d, the *k*-points corresponding to translation symmetries preserved along the (100) and (120) edges are marked by the blue and green lines, respectively. The calculated edge states with SOC, displayed in Fig. 2e, reveal a Dirac cone along the (100) direction. This observation confirms the presence of a topological metal phase in the BaCu monolayer.

Given its metallic nature, as indicated by $N(E_F) \sim 1.61$ states/eV/f.u. from TDOS, the superconducting properties of the BaCu monolayer were investigated. However, the results reveal that it does not exhibit conventional superconductivity, with a negligible critical temperature (T_c) at ambient pressure. This can be attributed to the presence of heavy elements, which result in a very low logarithmic average phonon frequency (ω_{log}) about 64.9 cm^{-1} and a weak electron-phonon coupling constant (λ) of about 0.21(for MgB_2, the $N(E_F) = 0.37$ states/eV/f.u., the $\omega_{log} = 740.3$ cm^{-1} and the $\lambda = 0.69$[49]). Although the BaCu monolayer does not exhibit intrinsic superconductivity, previous studies have reported that applying a 10% biaxial tensile strain can induce a superconducting phase with T_c of approximately 0.2 K[50]. This demonstrates that strain engineering could serve as an effective approach for modulating the electronic properties of the BaCu monolayer and realizing a superconducting phase transition. Furthermore, the effect of increasing the number of BaCu layers was examined. This multilayer configuration leads to a more complex charge distribution and band structure, as shown in Fig. S2. Importantly, these changes disrupt the topological property observed in the monolayer, highlighting the sensitivity of these features to the dimensionality and structural configuration of the material.

Twisted heterobilayer α-BaCu/BN

Given the intriguing properties of the BaCu monolayer, which is a 2D TI with a weak IAEs honeycomb network on its surface, it is worth exploring whether twisted heterostructures incorporating BaCu and other classical 2D materials might yield additional fascinating physics. To explore this possibility, we construct a twisted BaCu/h-BN heterostructure, selecting h-BN as the substrate due to its wide band gap (~4.9 eV[51]) and semiconducting nature. Given the strong metallic character of the BaCu monolayer discussed above, h-BN provides an ideal insulating counterpart for investigating interfacial effects in the heterostructure. Among various configurations, the heterostructure with a 30° twist angle exhibits the simplest crystal structure and the smallest atomic count. This system comprises a 1 × 1 BaCu monolayer and a $\sqrt{3} \times \sqrt{3}$ supercell of h-BN, resulting in a stoichiometric composition of $B_{1.5}N_{1.5}BaCu$. The lattice mismatch between the two layers is less than 0.5%, ensuring structural compatibility. Despite the absence of a moiré superlattice due to the large twist angle, the BaCu/h-

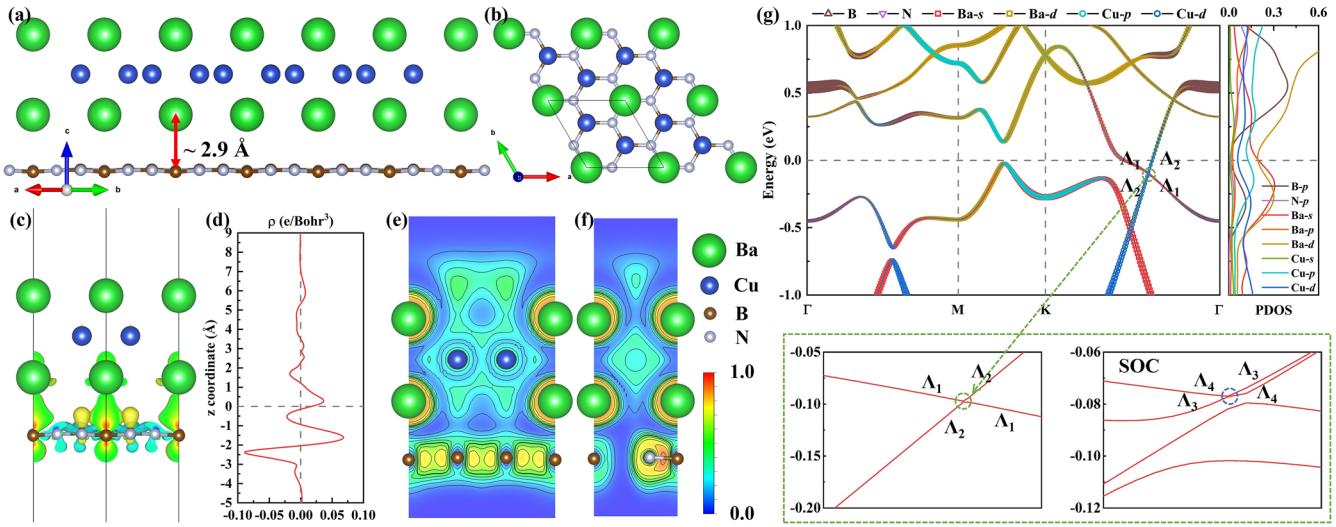

Fig. 3 | Crystal structure, electronic and topological band analysis of α-BaCu/BN. The structure of α-BaCu/BN with **a** side and **b** top view. **c** CDD between its two layers of it in side view with the isosurface values of 10^{-3} e/Bohr^3 and **d** the corresponding *ab*-plane-averaged charge density difference. The ELF contours of α-BaCu/BN on **e** (110) and **f** (-110) planes with the 0.1 linear divide. **g** The orbital-projected band structure and PDOS (states/eV/f.u.) of α-BaCu/BN with the calculated local area band structures without/with SOC.

BN heterostructure demonstrates distinctive topological band properties, highlighting its potential for uncovering new quantum phenomena.

Determined through systematic scanning of the relative slip and interlayer distance between the BaCu and h-BN layers in heterobilayer (Fig. S3), the energetically favorable configuration is designated as α-BaCu/BN. Its configuration with a layer group of LG.70 and a corresponding space group of *P*31*m* (SG.157), as shown in Fig. 3a, b, the optimized lattice parameters are a = b ≈ 4.355 Å, with an interlayer spacing of 2.9 Å. The h-BN layer in this configuration displays a minor "wrinkle" with a displacement amplitude of less than 0.111 Å, as shown in Fig. 3a, which arises from interlayer interactions. In the α-BaCu/BN structure, boron atoms occupy the 1a (0,0,0.381) and 2b (0.667,0.333,0.384) Wyckoff positions, while nitrogen atoms are located at the 3c (0,0.331,0.383) Wyckoff positions. The thermodynamic stability of this twisted BaCu/h-BN heterostructure is confirmed by its calculated formation energy of about −85.2 meV/atom. The formation energy is defined as U_f(α-BaCu/BN) = [U(α-BaCu/BN) − U(BaCu monolayer) − 3 × U(h-BN monolayer)]/10, where the terms represent the total energies of the heterobilayer and two constituent monolayers, respectively. Additionally, the absence of imaginary frequencies in the phonon spectrum (Fig. S1d) at 0 GPa and the retention of structural integrity during AIMD simulations at 0 GPa and both 300 K and 1000 K (Fig. S1e, f) further confirm that α-BaCu/BN is both dynamically and thermally stable.

Charge density difference (CDD) between the two layers (Fig. 3c) reveals that electron depletion primarily occurs near the h-BN layer. As shown in Fig. 3d, the h-BN layer donates charge along the *c*-axis, influencing the interlayer interaction. Compared to the BaCu monolayer, the IAEs are altered due to interlayer effects, with partial charge transfer observed above the B atoms. WF decreases slightly from 2.66 eV for the BaCu monolayer to 2.48 eV for α-BaCu/BN, reflecting its subtle electronic modifications. Although these changes in charge density are relatively minor (10^{-3} e/Bohr^3), they alter the local electronic distribution (Fig. 3e, f), leading to a reduction in the $N(E_F)$ from ~1.61 states/eV/f.u. for the BaCu monolayer to ~1.27 states/eV/f.u. for α-BaCu/BN. These variations are accompanied by slight shifts in the band structure (Fig. 3g), as anticipated.

As shown in Fig. 3g, the orbital-resolved band structures show a pronounced band inversion between the Ba-*s* and Cu-*d* dominated bands, resulting in a band crossing along the Γ-K direction, protected by M_{110} symmetry. Due to R_{3z} symmetry, this crossing generates three 2D Dirac points, which are related by the same symmetry. TRS further introduces three additional Dirac points along Γ-K′. When SOC is included, these Dirac points split due to the absence of inversion symmetry. A detailed band scan (inset Fig. 3g) shows negligible SOC-induced splitting for the Cu-*d* band, while a visible splitting is observed for the Ba-*s* band due to the large SOC of Ba atoms. Consequently, each Dirac point evolves into a Weyl point, forming three pairs of Weyl points with opposite chirality along Γ-K and Γ-K′, respectively. The twist operation which heterojunction construction apparently affects the topology characteristics.

Adjusted heterobilayer β-BaCu/BN

Tuning the relative sliding[52] and interlayer spacing[53] between neighboring layers is effective method for engineering the band structures in vdW heterostructures. We considered a local minimum structure with Ba and Cu atoms aligned to honeycomb voids of h-BN (named as β-BaCu/BN). The energy of β-BaCu/BN is just larger ~0.9 meV/atom than α-BaCu/BN, exhibits unique type-III Dirac points. The optimized structure of β-BaCu/BN, shown in Fig. 4a, b, retains the same layer group (LG.70) and space group (SG.157) as α-BaCu/BN. However, it exhibits slightly adjusted lattice parameters (a = b ≈ 4.354 Å) and an increased interlayer spacing of ~3.076 Å. Within β-BaCu/BN, the boron and nitrogen atoms occupy the 3c Wyckoff positions at coordinates (0.665,0.665,0.361) and (0.331,0.331,0.362), respectively. Interestingly, the AIMD simulations at 0 GPa and 300 K reveal a spontaneous shift of the h-BN layer along the [110] direction to the configuration of α-BaCu/BN (Fig. 4c) within 0.6 ps (Fig. 4d-i). This spontaneous shift suggests a low energy barrier between α and β phases, indicating experimental feasibility of structural modulation.

The CDD between BaCu and h-BN layers in β-BaCu/BN (Fig. 5a) shows some differences in charge transfer with the α-phase. Above B atoms, the obtained charge is tilted, which is contributed by the slip operation, B and Ba atoms are not strictly arranged along the *c*-axis now. But the global charge transfer can only see a subtle decrease (Fig. 5b), consistent with its larger interlayer spacing (3.067 Å). Overall, the structural differences lead to the variation in electron distribution (Fig. 5c, d). These give rise to the distinct type-III Dirac points in β-BaCu/BN, as shown in Fig. 5e.

Like the α-BaCu/BN, β-BaCu/BN also hold a band crossing along the Γ-K direction protected by M_{110} symmetry and generates three 2D Dirac points through R_{3z} symmetry. Differently, the nearly dispersionless Ba-dominated bands along Γ-K contribute to these crossings, classifying them as type-III Dirac points—a critical state between type-I and type-II Dirac fermions, characterized by a Dirac cone touching the E_F at its surface. The Dirac point is located at (k_c, k_c) where $k_c = 0.128\frac{2\pi}{a}$, with a representing the lattice constant. In addition, similar with the 2D Mn_3Sn system, the flat band

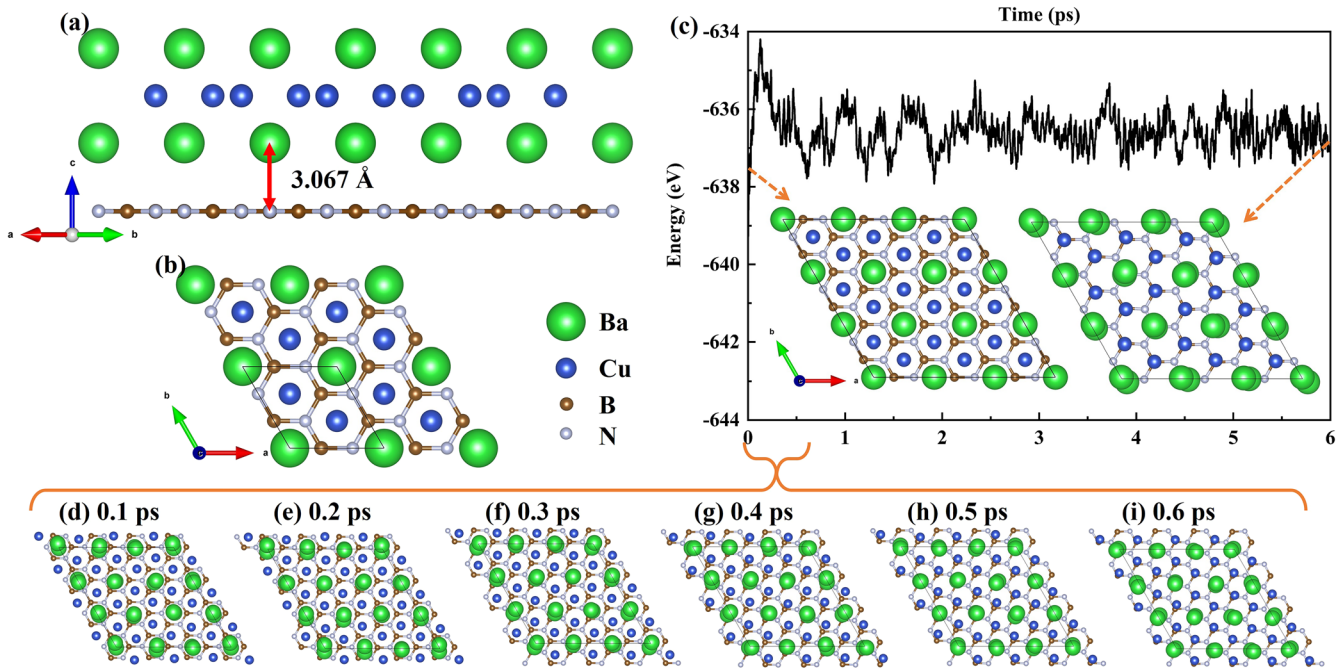

Fig. 4 | Crystal structure of β-BaCu/BN and its spontaneous transition in AIMD simulation. The structure of β-BaCu/BN in **a** side and **b** top view. **c** AIMD of β-BaCu/BN at 0 GPa 300 K with the initial and final structures, and **d**–**i** the spontaneous shifted process captured from 0.1 to 0.6 ps.

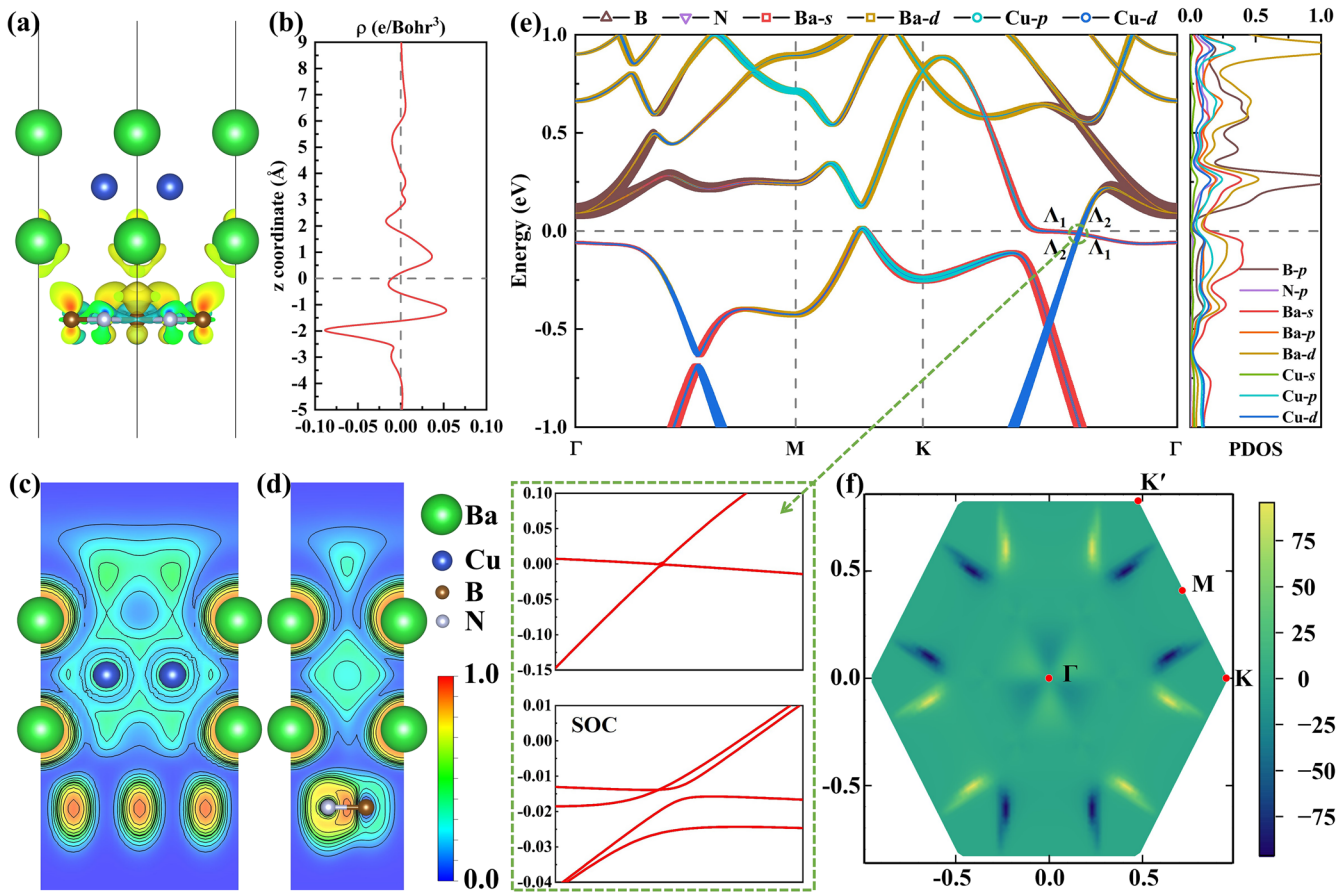

Fig. 5 | Crystal structure, electronic and topological scanning analysis of β-BaCu/BN. a The CDD between two layers of β-BaCu/BN in side view with the isosurface values of 10^{-3} e/Bohr^3 and **b** the corresponding *ab*-plane-averaged charge density difference. The ELF contours of β-BaCu/BN on **c** (110) and **d** (-110) planes with the 0.1 linear divide. **e** The orbital-projected band structure and PDOS (states/eV/f.u.) of β-BaCu/BN with the calculated local area band structures without/with SOC. **f** Berry curvature density of β-BaCu/BN.

contributed to the type-III Dirac point near the E_F remind us of the potential existence of the kondo lattice and kondo effect in the 2D (twisted) system[54–57]. When SOC is introduced, these Dirac points become gapped, as illustrated inset Fig. 5e. However, detailed band scanning with finer *k*-point spacing reveals that the SOC-induced gap is minimal (~3.9 meV), underscoring the robustness of type-III Dirac fermions in this system. The Berry curvature density plot (Fig. 5f) further corroborates the existence of type-III Dirac points. Distinct *k*-points exhibiting maximum positive and minimum negative Berry curvature are observed near the Dirac points, providing additional verification of their presence and properties. Since the PBE functional tends to underestimate band gaps, we also calculate the local band structures with the Heyd–Scuseria–Ernzerhof hybrid exchange–correlation functional (HSE06)[58], as shown in Fig. S4. The energy dispersions at the band crossing points from HSE06 are similar to those from PBE, confirming the robustness of the topological characteristics. In addition, we calculate the corresponding edge states for both the α- and β-twisted systems (Fig. S5), comparing the band structures obtained from the Wannier-based tight-binding model with those from first-principles DFT calculations. The close agreement between the two methods confirms the reliability of our data.

In summary, we have investigated the stability, electronic structures, and topological properties of the BaCu monolayer and the twisted α/β-BaCu/BN heterostructures. These twisted heterostructures consist of a BaCu monolayer stacking on a $\sqrt{3} \times \sqrt{3}$ supercell of the h-BN monolayer, twisted by 30°. Although this large twist angle prevents the formation of moiré superlattice, the resulting heterostructures exhibit unique topological band characteristics. First-principles calculations reveal that the BaCu monolayer is a nodal line semimetal without SOC, transitioning to a topological metal with 2D TI features when SOC is included. Attributed to the heavy mass of Ba and Cu, the calculated T_c based on BCS theory is negligible. Furthermore, the 30° twisted bilayer α-BaCu/BN hosts six Weyl points, demonstrating that twisting can effectively tune topological properties. Considered the adjust of relative sliding and interlayer spacing between neighboring layers can effectively modulate the electronic property in vdW heterostructures, β-BaCu/BN with Ba and Cu atoms aligned to the honeycomb voids of h-BN is picked out. Its energy lager then α-BaCu/BN ~ 0.9 meV/atom, with lager larger interlayer spacing (~3.067 Å, α-BaCu/BN ~ 2.9 Å). Notably, AIMD simulations performed at 0 GPa and 300 K reveal a spontaneous transition from the metastable β-BaCu/BN to α-BaCu/BN, indicating a low potential barrier between these structures and the feasibility of modulating this twisted heterobilayer. The β-BaCu/BN configuration exhibits unique type-III Dirac points at the E_F, highlighting the potential of twisted structures to modulate topological properties. This work establishes a robust theoretical and experimental platform for exploring twist-angle-induced topological electride states, offering broad opportunity for further research in tailored topological materials.

Methods

Density functional theory calculations

Calculations of the structural relaxations and electronic band structure are performed under the frame of the density functional theory integrated in the Vienna ab initio simulations package (VASP)[59]. The exchange–correlation functional is given by the generalized gradient approximation parameterized by Perdew, Burke, and Ernzerhof[60]. The van der Waals interactions were explicitly included in all VASP calculations by adopting the DFT-D4[61] functional. The plane-wave cutoff energy of 600 eV and Monkhorst–Pack *k* meshes with a grid spacing of $2\pi \times 0.02$ Å^{-1} were adopted. The dynamic stabilities were verified by calculations of the phonon spectra using the direct supercell method with PHONOPY code[62]. Ab initio molecular dynamics (AIMD) simulations were carried out using the Nosé–Hoover chain thermostat with the temperature of 300 K for 6 ps with a time step of 1 fs. The WF value was calculated through the formula of $\Phi_{WF} = E_{vac} - E_F$ (E_{vac} is vacuum level, E_F is Fermi level). The IRVSP[63] were used for the irreducible representations. The Berry curvature is calculated from wavefunctions derived via first-principles methods[64,65].

Data availability

The authors declare that the main data supporting the findings of this study are available within the article and its Supplementary Information files.

Code availability

The code for calculations can be found at VASP - Vienna Ab initio Simulation Package with Kresse, G., Furthmüller, *J. Comput. Mater. Sci.* **6**, 15-50 (1996). The version of the code employed for this study is version 6.3.0. The code to obtain irreducible representations can be found at IRVSP with Gao, J., Wu, Q., Persson, C. and Wang, Z. *Comput. Phys. Comm.* **261**, 107760 (2021).

Received: 31 January 2025; Accepted: 24 June 2025;
Published online: 08 July 2025

References

1. Novoselov, K. S. et al. Electric field effect in atomically thin carbon films. *Science* **306**, 666–669 (2004).
2. Novoselov, K. S. et al. Two-dimensional atomic crystals. *Proc. Natl. Acad. Sci. USA* **102**, 10451–10453 (2005).
3. Geim, A. K. Graphene: status and prospects. *Science* **324**, 1530–1534 (2009).
4. Wang, Q. H., Kalantar-Zadeh, K., Kis, A., Coleman, J. N. & Strano, M. S. Electronics and optoelectronics of two-dimensional transition metal dichalcogenides. *Nat. Nanotechnol.* **7**, 699–712 (2012).
5. Novoselov, K. S., Mishchenko, A., Carvalho, A. & Castro Neto, A. H. 2D materials and van der Waals heterostructures. *Science*. **353**, aac9439 (2016).
6. Geim, A. K. & Grigorieva, I. V. Van der Waals heterostructures. *Nature* **499**, 419–425 (2013).
7. Cao, Y. et al. Unconventional superconductivity in magic-angle graphene superlattices. *Nature* **556**, 43–50 (2018).
8. Cao, Y. et al. Correlated insulator behaviour at half-filling in magic-angle graphene superlattices. *Nature* **556**, 80–84 (2018).
9. Cheng, Y., Huang, C., Hong, H., Zhao, Z. & Liu, K. Emerging properties of two-dimensional twisted bilayer materials. *Chinese Phys. B* **28**, 107304 (2019).
10. He, F. et al. Moiré Patterns in 2D materials: a review. *ACS Nano* **15**, 5944–5958 (2021).
11. Wang, L. et al. Correlated electronic phases in twisted bilayer transition metal dichalcogenides. *Nat. Mater.* **19**, 861–866 (2020).
12. An, L. et al. Interaction effects and superconductivity signatures in twisted double-bilayer WSe_2. *Nanoscale Horiz.* **5**, 1309–1316 (2020).
13. Wu, F., Lovorn, T. & Macdonald, A. H. Topological exciton bands in Moiré hHeterojunctions. *Phys. Rev. Lett.* **118**, 1–6 (2017).
14. Huang, S. et al. Topologically protected helical states in minimally twisted bilayer graphene. *Phys. Rev. Lett.* **121**, 37702 (2018).
15. Choi, Y. et al. Correlation-driven topological phases in magic-angle twisted bilayer graphene. *Nature* **589**, 536–541 (2021).
16. Can, O. et al. High-temperature topological superconductivity in twisted double-layer copper oxides. *Nat. Phys.* **17**, 519–524 (2021).
17. Kane, C. L. & Mele, E. J. Quantum spin hall effect in graphene. *Phys. Rev. Lett.* **95**, 226801 (2005).
18. Liu, C., Hughes, T. L., Qi, X.-L., Wang, K. & Zhang, S.-C. Quantum spin hall effect in inverted type-II semiconductors. *Phys. Rev. Lett.* **100**, 236601 (2008).
19. Knez, I., Du, R.-R. & Sullivan, G. Evidence for helical edge modes in inverted InAs/GaSb quantum wells. *Phys. Rev. Lett.* **107**, 136603 (2011).
20. Qian, X., Liu, J., Fu, L. & Li, J. Quantum spin hall effect in two-dimensional transition metal dichalcogenides. *Science* **346**, 1344–1347 (2014).
21. Kou, L., Ma, Y., Sun, Z., Heine, T. & Chen, C. Two-dimensional topological insulators: progress and prospects. *J. Phys. Chem. Lett.* **8**, 1905–1919 (2017).
22. Kane, C. L. & Mele, E. J. Z_2 Topological order and the quantum spin hall effect. *Phys. Rev. Lett.* **95**, 146802 (2005).

23. Bernevig, B. A. & Zhang, S.-C. Quantum spin hall effect. *Phys. Rev. Lett.* **96**, 106802 (2006).
24. Bernevig, B. A., Hughes, T. L. & Zhang, S.-C. Quantum spin hall effect and topological phase transition in HgTe quantum wells. *Science* **314**, 1757–1761 (2006).
25. König, M. et al. Quantum spin hall insulator state in HgTe quantum wells. *Science* **318**, 766–770 (2007).
26. Li, X.-G. et al. Proximity effects in topological insulator heterostructures. *Chin. Phys. B* **22**, 097306 (2013).
27. Kou, L. et al. Robust 2D topological insulators in van der Waals heterostructures. *ACS Nano* **8**, 10448–10454 (2014).
28. Kezilebieke, S. et al. Topological superconductivity in a van der Waals heterostructure. *Nature* **588**, 424–428 (2020).
29. Bazarnik, M. et al. Antiferromagnetism-driven two-dimensional topological nodal-point superconductivity. *Nat. Commun.* **14**, 614 (2023).
30. Kou, L. et al. Graphene-based topological insulator with an intrinsic bulk band gap above room temperature. *Nano Lett.* **13**, 6251–6255 (2013).
31. Chu, R.-L. et al. Spin-orbit-coupled quantum wires and Majorana fermions on zigzag edges of monolayer transition-metal dichalcogenides. *Phys. Rev. B* **89**, 155317 (2014).
32. Xu, G., Wang, J., Yan, B. & Qi, X.-L. Topological superconductivity at the edge of transition-metal dichalcogenides. *Phys. Rev. B* **90**, 100505 (2014).
33. Wan, B. et al. BaCu, a two-dimensional electride with Cu anions. *J. Am. Chem. Soc.* **146**, 17508–17516 (2024).
34. Lee, K., Kim, S. W., Toda, Y., Matsuishi, S. & Hosono, H. Dicalcium nitride as a two-dimensional electride with an anionic electron layer. *Nature* **494**, 336–340 (2013).
35. Druffel, D. L. et al. Experimental demonstration of an electride as a 2D material. *J. Am. Chem. Soc.* **138**, 16089–16094 (2016).
36. Cao, G., Zhang, S., Cui, P. & Zhang, Z. Enhanced Itinerant d_0 Ferromagnetism and tunable topological properties of a Ca_2C/Ca_2N heterobilayer. *Adv. Electron. Mater.* **10**, 1–8 (2024).
37. Fang, C., Weng, H., Dai, X. & Fang, Z. Topological nodal line semimetals. *Chin. Phys. B* **25**, 117106 (2016).
38. Guo, Z. et al. Quantum spin hall effect in $Ta_2M_3Te_5$ (M = Pd, Ni). *Phys. Rev. B* **103**, 115145 (2020).
39. Wang, X. et al. Observation of topological edge states in the quantum spin Hall insulator $Ta_2Pd_3Te_5$. *Phys. Rev. B* **104**, L241408 (2021).
40. Zhang, H. et al. Topological insulators in Bi_2Se_3, Bi_2Te_3 and Sb_2Te_3 with a single Dirac cone on the surface. *Nat. Phys.* **5**, 438–442 (2009).
41. Shao, D. et al. Topological insulators in the NaCaBi family with large spin-orbit coupling gaps. *Phys. Rev. Res.* **3**, 013278 (2021).
42. Shao, D. & Fang, C. Filling-enforced Dirac nodal loops in nonmagnetic systems and their evolutions under various perturbations. *Phys. Rev. B* **102**, 165135 (2020).
43. Song, Z., Zhang, T., Fang, Z. & Fang, C. Quantitative mappings between symmetry and topology in solids. *Nat. Commun*. **9**, 3530 (2018).
44. Khalaf, E., Po, H. C., Vishwanath, A. & Watanabe, H. Symmetry indicators and anomalous surface states of topological crystalline insulators. *Phys. Rev. X* **8**, 31070 (2018).
45. Song, Z., Huang, S.-J., Qi, Y., Fang, C. & Hermele, M. Topological states from topological crystals. *Sci. Adv.* **5**, 1–13 (2019).
46. Fu, L. & Kane, C. L. Topological insulators with inversion symmetry. *Phys. Rev. B* **76**, 045302 (2007).
47. Pizzi, G. et al. Wannier90 as a community code: new features and applications. *J. Phys. Condens. Matter* **32**, 165902 (2020).
48. Wu, Q., Zhang, S., Song, H.-F., Troyer, M. & Soluyanov, A. A. WannierTools: an open-source software package for novel topological materials. *Comput. Phys. Commun.* **224**, 405–416 (2018).
49. Liao, J.-H., Zhao, Y.-C., Zhao, Y.-J., Xu, H. & Yang, X.-B. Phonon-mediated superconductivity in Mg intercalated bilayer borophenes. *Phys. Chem. Chem. Phys.* **19**, 29237–29243 (2017).
50. Zhou, T., Guan, Z., Cui, T. & Li, D. Strain-induced interstitial anionic electrons and superconductivity of monolayer BaCu. *Supercond. Sci. Technol.* **38**, 015018 (2025).
51. Satawara, A. M., Shaikh, G. A., Gupta, S. K. & Gajjar, P. N. Structural, electronic and optical properties of hexagonal boron-nitride (h-BN) monolayer: an ab-initio study. *Mater. Today Proc.* **47**, 529–532 (2021).
52. Fox, C., Mao, Y., Zhang, X., Wang, Y. & Xiao, J. Stacking order engineering of two-dimensional materials and device applications. *Chem. Rev.* **124**, 1862–1898 (2024).
53. Ding, Y. et al. Bidirectional and reversible tuning of the interlayer spacing of two-dimensional materials. *Nat. Commun.* **12**, 1–7 (2021).
54. Demsar, J., Sarrao, J. L. & Taylor, A. J. Dynamics of photoexcited quasiparticles in heavy electron compounds. *J. Phys. Condens. Matter* **18**, R281–R314 (2006).
55. Zhang, S. S. et al. Many-body resonance in a correlated topological Kagome antiferromagnet. *Phys. Rev. Lett.* **125**, 46401 (2020).
56. Shen, S. et al. Inducing and tuning Kondo screening in a narrow-electronic-band system. *Nat. Commun.* **13**, 1–7 (2022).
57. Song, Z. D. A. & Bernevig, B. A. Magic-angle twisted bilayer graphene as a topological heavy fermion problem. *Phys. Rev. Lett.* **129**, 47601 (2022).
58. Heyd, J., Scuseria, G. E. & Ernzerhof, M. Hybrid functionals based on a screened Coulomb potential. *J. Chem. Phys.* **118**, 8207–8215 (2003).
59. Kohn, W. & Sham, L. J. Self-consistent equations including exchange and correlation effects. *Phys. Rev.* **140**, A1133–A1138 (1965).
60. Perdew, J. P., Burke, K. & Ernzerhof, M. Generalized gradient approximation made simple. *Phys. Rev. Lett.* **77**, 3865–3868 (1996).
61. Caldeweyher, E., Mewes, J.-M., Ehlert, S. & Grimme, S. Extension and evaluation of the D4 London-dispersion model for periodic systems. *Phys. Chem. Chem. Phys* **22**, 8499–8512 (2020).
62. Togo, A. First-principles phonon calculations with Phonopy and Phono3py. *J. Phys. Soc. Japan* **92**, 012001 (2023).
63. Gao, J., Wu, Q., Persson, C. & Wang, Z. Irvsp: To obtain irreducible representations of electronic states in the VASP. *Comput. Phys. Commun.* **261**, 107760 (2021).
64. Kim, S. et al. Direct measurement of the quantum metric tensor in solids. *Science* **388**, 1050–1054.
65. Kim, H. J. VASPBERRY. https://github.com/Infant83/VASPBERRY.

Acknowledgements

The authors acknowledge funding support from the National Natural Science Foundation of China (Grants No. 12074013, No. 12204138 and No. 12204419), the National Science Fund for Distinguished Young Scholars (Grant No. T2225027). The calculations were carried out using supercomputers at the Hefei Advanced Computing Center. We also thank for the fruitful discussions with Rui Wang and Zhaopeng Guo.

Author contributions

H.G., D.S., B.W. and Y.L. conceived and designed the study. B.W. performed preliminary calculations. Y.L. performed the first principles calculations, data analysis, investigation, and wrote the manuscript. H.G. and D.S. performed the supervision and writing-review and editing. X.L. and Y.J. and Y.Q. performed the topological properties calculations and corresponding data analysis. All authors read and approved the final manuscript.

Competing interests

The authors declare no competing interests.

Additional information

Supplementary information The online version contains supplementary material available at https://doi.org/10.1038/s41524-025-01716-0.

Correspondence and requests for materials should be addressed to Biao Wan, Dexi Shao or Huiyang Gou.